Molecular dynamics of a grid-mounted molecular dipolar rotor in a rotating electric field

Jaroslav Vacek* and Josef Michl†‡

*J. Heyrovský Institute of Physical Chemistry, Academy of Sciences of the Czech Republic, Dolejškova 3, 182 23, Prague 8, Czech Republic; and †Department of Chemistry and Biochemistry, University of Colorado, Boulder, CO 80309-0215

Contributed by Josef Michl, February 28, 2001

Classical molecular dynamics is applied to the rotation of a dipolar molecular rotor mounted on a square grid and driven by rotating electric field $E(\nu)$ at $T \simeq 150$ K. The rotor is a complex of Re with two substituted *o*-phenanthrolines, one positively and one negatively charged, attached to an axial position of Rh_2^{4+} in a [2]staffanedicarboxylate grid through 2-(3-cyanobicyclo[1.1.1]pent-1-yl)malonic dialdehyde. Four regimes are characterized by a, the average lag per turn: (*i*) synchronous ($a < 1/e$) at $E(\nu) = |E(\nu)| > E_c(\nu)$ [$E_c(\nu)$ is the critical field strength], (*ii*) asynchronous ($1/e < a < 1$) at $E_c(\nu) > E(\nu) > E_{bo}(\nu) > kT/\mu$, [$E_{bo}(\nu)$ is the break-off field strength], (*iii*) random driven ($a \simeq 1$) at $E_{bo}(\nu) > E(\nu) > kT/\mu$, and (*iv*) random thermal ($a \simeq 1$) at $kT/\mu > E(\nu)$. A fifth regime, (v) strongly hindered, $W > kT$, $E\mu$, (W is the rotational barrier), has not been examined. We find $E_{bo}(\nu)/\text{kVcm}^{-1} \simeq (kT/\mu)/\text{kVcm}^{-1} + 0.13(\nu/\text{GHz})^{1.9}$ and $E_c(\nu)/\text{kVcm}^{-1} \simeq (2.3kT/\mu)/\text{kVcm}^{-1} + 0.87(\nu/\text{GHz})^{1.6}$. For $\nu > 40$ GHz, the rotor behaves as a macroscopic body with a friction constant proportional to frequency, $\eta/\text{eVps} \simeq 1.14\ \nu/\text{THz}$, and for $\nu < 20$ GHz, it exhibits a uniquely molecular behavior.

Molecular construction kits promise access to giant molecules shaped like regular grids and scaffolds carrying active and/or mobile groups (1–4). A sturdy artificial square grid polymer, albeit irregular and only ~150 nm across, has been reported (5, 6), and time appears right to use computer simulation of these "designer solids" to analyze the role of thermal motion in molecular machinery and to identify the best synthetic targets.

One of the active elements proposed (4, 7) for incorporation in these molecular scaffolds is a dipolar rotor, capable of rotational motion in response to an outside driving force. Molecular rotors driven unidirectionally by light (8), or bidirectionally by heat (9–12) or chemically (13, 14) have been synthesized. Alternating electric field has been used to affect intramolecular motion (15), and intense laser field of rapidly rotating linear polarization has been used to drive the rotation of a chlorine molecule (16). Free hydroxyl groups on oxide surfaces behave as two-dimensional arrays of interacting rotors, as do phospholipids in certain membranes and dipolar molecules adsorbed on flat surfaces or intercalated in layered solids (17). Biological motors (18) are under study. The velocity at which a dissolved chiral molecule is propelled through a solution by circularly polarized microwaves has been theoretically estimated (19–21).

Previously (22), we examined computationally the unidirectional motion of a grid-mounted propeller-shaped rotor driven by a stream of gas. This windmill rotor acted as a microphone, transducing linear motion of gas molecules into rotational motion of electric charges. A propeller-shaped rotor driven by a rotating electric field in the presence of a gas might produce a pressure differential, acting as a loudspeaker or a gas pump.

The dielectric response of a dipolar rotor is intrinsically nonlinear and therefore theoretically and possibly even practically interesting. Analyses (23–25) of a one-dimensional string of rotors interacting by electrostatic forces suggest that solitary waves may be possible. Such analyses benefit from a phenomenological characterization of the rotor, e.g., by its friction constant. The statistical physics of interacting rotors in two dimensions is likely to be of special importance (17), considering the strong current interest in two-dimensional spin glasses (26).

We examine the motion of a single dipolar rotor mounted on a square grid and driven in vacuum by a rotating electric field. Two prior studies (27, 28) simulated the motion of a dipolar rotor consisting of two concentric carbon nanotubes in a linearly oscillating electric field. Our work differs in several respects: (*i*) the synthesis of our rotor is feasible by procedures known today, (*ii*) the propeller is mounted on a molecular grid, (*iii*) we use a rotating electric field, avoiding the irregular changes in the sense of rotation that dominated the earlier results, (*iv*) we apply much weaker fields, and (*v*) we fit a model to the results and extract a value of an effective friction constant.

We use the smaller of the rotors and the finer of the grids described previously (22) (Fig. 1). The dipole moment of the rotor $\mu = |\boldsymbol{\mu}|$ is ~42 debye, its moment of inertia I is $\sim 1.5 \times 10^4$ $u\text{Å}^2$ (u is the atomic mass unit), and its 4-fold rotational barrier on the grid is $W = 0.3 \pm 0.2$ kcal/mol. We vary the frequency ν (angular frequency $\omega = 2\pi\nu$, $\omega = |\boldsymbol{\omega}|$, with $\boldsymbol{\omega}$ directed in the positive sense of the rotation axis z) and the strength of the rotating electric field $E(\nu) = |\boldsymbol{E}(\nu)|$. Exploratory runs at various temperatures T showed that at 150 K the rotor behaves well, and further simulations were initiated at this temperature.

Method of Calculation

The classical molecular dynamics computer program uses the UFF potential energy and charge equilibration scheme of Rappé *et al.* (29, 30), which ignores polarization and treats all elements in the periodic table at the cost of reduced accuracy. It does not correct for the negligible radiative losses due to moving charges, nor for quantum mechanical effects, which are of unknown magnitude but are not expected to change the results qualitatively. We did not try to compensate for the latter by freezing high-frequency motions of C—H bonds, which probably causes friction to be overestimated, whereas the finite size of the modeled grid causes it to be underestimated.

The square grid fragment modeled (Fig. 1) consisted of 12 rods, [2]staffanes terminally substituted with two carboxylates (4), attached to nine dirhodium tetracation (31, 32) connectors whose axial positions were occupied by CH_3CN ligands on top and HCN ligands at the bottom, except for the central bottom position used to hold the nitrile group at the end of the propeller axis. The rotor has been described in ref. 22. The axial attachment of the nitrile group to rhodium is weak but adequate for the length of the simulation runs used. No dissociation events were observed when a Morse potential was used for the Rh—N bond. In practice, the structures used will need to be stable indefinitely at the operating temperature.

CHEMISTRY

Abbreviation: JJ, Josephson junction.

‡To whom reprint requests should be addressed. E-mail: michl@eefus.colorado.edu.

The publication costs of this article were defrayed in part by page charge payment. This article must therefore be hereby marked "*advertisement*" in accordance with 18 U.S.C. §1734 solely to indicate this fact.

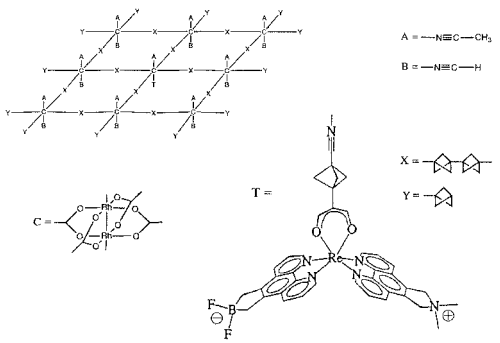

Fig. 1. Chemical structures of the rotor (T) and the supporting grid. The structures of the constituent modules, A, B, C, X, and Y, are shown separately.

The computational procedure (22) was simplified by the absence of gas atoms. Constant energy molecular dynamics with external electric field was used (no velocity scaling). Before simulation, the molecular structures were well optimized by using truncated Newton optimization. As usual, initial velocities were assigned according to a Maxwell-Boltzmann velocity distribution. Different starting geometries and velocity distributions were used in some simulations to sample more space. The actual initial temperatures therefore differed slightly from 150 K and from one run to another. Integration time steps of 1.1, 1.8, and 2.8 fs were tested and gave the same results; thereafter, the step was fixed at 2.1 fs. A typical total run time t_{tot} was sufficient for 5–350 full revolutions of the electric field vector $\boldsymbol{E}$ (0.1–3.5 ns, most often 0.5–1 ns). The total simulated time was over 100 ns (171 runs).

The rotational barrier W was calculated as the energy difference of the whole structure at a geometry optimized with the angle between the rotor dipole and the grid rods constrained once at 0 and once at 45°. To obtain sufficient accuracy it was essential to use a 50-Å cutoff for electrostatic interactions; in the molecular dynamics runs the cutoff was 30 Å.

The effect of an external grid support was modeled by fixing the position of the Rh atom to which the rotor axle is attached (the origin of the coordinate system), and constraining the 12 bridgehead H atoms at the grid periphery to the xy plane. The homogeneous external electric field $\boldsymbol{E}$ rotated around the z axis and its components were $E_x = E\sin(\omega t + \pi/4)$, $E_y = E\cos(\omega t + \pi/4)$, $E_z = 0$, where t is time. The dipole was initially oriented along the y axis. Time averages $\langle q\rangle = t_{\rm tot}^{-1}\int q(t)dt$ of various properties q were calculated separately over each run of duration $t_{\rm tot}$. The properties monitored were the temperature of the rotor $T_{\rm r}(t)$ (overall rotation of the rotor was subtracted from the motion of the atoms, *cf.* ref. 22) and of the grid $T_{\rm g}(t)$, the z components of the rotor angular momentum $M_z(t)$ and moment of inertia $I_z(t)$, the projection of the rotor dipole moment into the xy plane $\boldsymbol{\mu}_{\rm xy}(t)$, the number of turns m the rotor was behind the field vector, and the cumulative angle $\alpha(t)$ ($-\infty < \alpha < \infty$) by which it lagged behind the driving electric field (measured between the projections of the dipole moment vector of the rotor $\boldsymbol{\mu}$ and of the rotating electric field vector $\boldsymbol{E}$ into the xy plane, positive when the rotor lags behind the field).

The performance of the rotor was judged by: (*i*) The mean lag per turn $a = \alpha_{\rm tot}/2\pi n$, where $\alpha_{\rm tot} = \alpha(t_{\rm tot})$ is the final value of the lag angle α after n turns of the field. (*ii*) The time-averaged lag angle $\langle\alpha\rangle$. (*iii*) The time-averaged lag per turn $a' = \langle\alpha\rangle/\pi n$ (similar to a; not used in the discussion). (*iv*) The average rotational frequency of the rotor $\nu_{\rm rot} = \langle M_z\rangle/(2\pi\langle I_z\rangle)$. (*v*) The rms fluctuation of the lag angle $\langle\Delta\alpha\rangle = (\langle\alpha^2\rangle - \langle\alpha\rangle^2)^{1/2}$. (*vi*) A measure of the average torque on the rotor, $\langle\sin\alpha\rangle$. (*vii*) A measure of the average polarization of the rotor in the rotating coordinate system, $\langle\cos\alpha\rangle$.

Results

Sample results are collected in Table 1. The average projection of the rotor dipole moment into the xy plane is $\boldsymbol{\mu}_{\rm xy} \simeq 41.6$ debye, and the average z component of the moment of inertia of the rotor is 1.5×10^4 uÅ^2, occasionally reaching values up to 4.5×10^4 uÅ^2, due to centrifugal forces, internal motion within the rotor, and its overall irregular pendular motion. Whereas $\mu_{\rm xy}$ grows only slightly with increasing rotational frequency, $\langle M_z\rangle$ is more sensitive to the mode of overall motion and often increases significantly with the rotational frequency. The $\langle M_z\rangle$ values are mostly negative, i.e., the rotor is moving in the same sense as the field. In most cases, the temperatures $T_{\rm r}(t)$ and $T_{\rm g}(t)$ remained equal to the initial temperature within a few K. A significant increase was generally observed only at frequency above 100 GHz at fields stronger than 3,000 kV·cm^{-1}. The highest observed temperature was 380 K. In longer simulations (~2 ns), however, a slight temperature increase by up to 20 K was observed even for weaker fields. No provision has been made to remove the heat generated. The actual average temperature was evaluated for each simulation and taken into account during the evaluation of the data.

At eight frequencies from 3.2 to 200 GHz, E was varied from 100 to 7,000 kV/cm, and at six field strengths from 430 to 5208 kV·cm^{-1}, ν was varied from 2 to 400 GHz (Table 1). Fig. 2 presents the rotor motion in four representative runs, and Fig.

Table 1. Examples of average rotor and grid properties (150 K)

Run	n	m	$t_{\rm tot}$, ps	$E/10^2$, kV·cm^{-1}	ν, GHz	$\nu_{\rm rot}$, GHz	a	a'	$\langle\alpha\rangle$, rad	$\langle\delta\alpha\rangle$, rad	$\langle M_z\rangle$, u·Å^2·rad·fs^{-1}	$\langle\sin\alpha\rangle$	$\langle\cos\alpha\rangle$
1	11.2	0	144	2,170	78	72	0	0	0.11	0.9	−5.66	0.07	0.67
2	11.2	5	144	1,736	78	46	0.48	0.29	10.4	12.8	−3.63	0.08	−0.02
3	11.2	3	144	1,302	78	78	0.25	0.18	6.52	6.5	−6.13	0.11	−0.07
4	11.2	6	144	1,085	78	52	0.56	0.38	13.5	10.7	−4.1	0.12	−0.07
5	22.5	16	287	651	78	27	0.73	0.9	63.4	32.7	−2.08	0.11	−0.15
6	5.6	0	287	1,736	19	26	0	0	0	0.5	−2.02	0.03	0.86
7	5.6	5	287	217	19	4	0.82	0.82	14.5	7.3	−0.32	0.1	0.18
8	6.6	8	2,011	108	3	1	1.2	1.26	26.2	13.8	+0.08	0.1	0.26
9	6.6	0	2,011	543	3	3	0	0	0	0.64	−0.25	0.01	0.82
10	13.5	0	1,034	1,519	13	11	0	0	0.1	0.5	−0.99	0.05	0.89
11	115	40	1,034	1,519	111	81	0.35	0.41	149	65.1	−7.38	0.16	0.17
12	155	146	1,034	1,519	150	11	0.94	1.01	489	287.3	−1.03	0	−0.07

n: number of field turns; m: number of turns skipped by rotor; $t_{\rm tot}$: simulation time; E: field strength; ν: field frequency; $\nu_{\rm rot}$: average rotor frequency; a: mean lag per turn; a': time averaged lag per turn; $\langle\alpha\rangle$: time averaged lag angle; $\langle\delta\alpha\rangle$: lag angle rms fluctuation; $\langle M_z\rangle$: average rotor angular momentum; $\langle\sin\alpha\rangle$ indicates average torque and $\langle\cos\alpha\rangle$, average polarization in rotating coordinates.

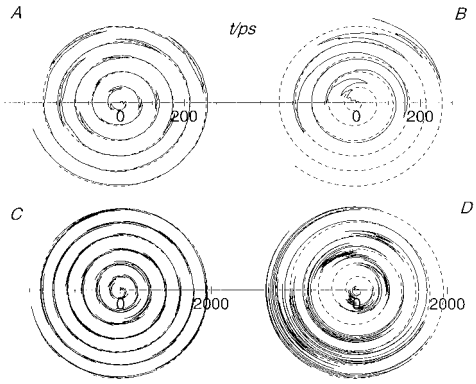

Fig. 2. Polar graphs of the time dependence of the dipole moment (solid lines) and electric field vector (dashed lines), *cf.* Table 1 (run number, *a*, *E* in kV·cm^{-1}, ν in GHz). (*A*) 6, −0.01, 1736, 19. (*B*) 7, 0.82, 217, 19. (*C*) 9, −0.01, 543, 3. (*D*) 8, 1.2, 108, 3.

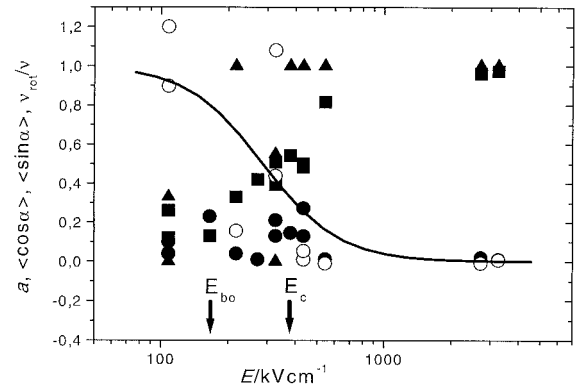

Fig. 4. Performance characteristics plotted against *E* at ν = 3 GHz: ○, *a*; ■, ⟨cosα⟩; ●, ⟨sinα⟩; ▲, ν_{rot}/ν. The solid line refers to *a* and serves merely as a guide for the eye.

3 shows the variation of $M_z(t)$ and $\alpha(t)$ in two of them. The dependence of four measures of rotor performance on E is similar at all frequencies. The results obtained at ν = 3 GHz are shown in Fig. 4. The estimated field strength above which a begins to deviate detectably from unity is denoted E_{bo}, and the critical field strength at which a drops below $1/e$ is denoted E_c. Within the accuracy of this determination, these field strengths could just as well be read off the plot of ⟨cosα⟩ or ν_{rot}/ν. The plot of ⟨sinα⟩ is too flat and less useful. There is an uncertainty in the definition of the break-off field E_{bo} unless the smallest deviation of a from unity that can be reliably detected is specified. This is a function of the length of the molecular dynamics runs; the uncertainty that pertains to the present results (Table 2) is marked by bars in Fig. 5.

The plots of log E_{bo} and log E_c against log ν (Fig. 5) are approximately linear above ~40 GHz; $E_{bo}(\nu)/\text{kV·cm}^{-1} \simeq (kT/\mu)/\text{kV·cm}^{-1} + 0.13(\nu/\text{GHz})^{1.9}$ and $E_c(\nu)/\text{kV·cm}^{-1} \simeq (2.3kT/\mu)/\text{kV·cm}^{-1} + 0.87(\nu/\text{GHz})^{1.6}$ (k is the Boltzmann constant, T = 150 K). Below ~40 GHz, E_{bo} becomes independent of the frequency, $E_{bo} \simeq kT/\mu$ = 140 kV·cm^{-1}, whereas E_c converges more slowly to a higher limit, $E_c(0) \simeq 2.3\ kT/\mu$. E_c is roughly equal to $2E_{bo}$ (ν); at the highest fields this ratio decreases.

In 35 additional runs we examined the field-free decay of the rotational motion. After a 15-ps period of thermal equilibration, additional velocity vectors corresponding to a rotational excitation at a frequency at 155 GHz in either direction were instantaneously assigned to all atoms of the rotor and the subsequent motion was monitored. The z component of the angular momentum decayed from its initial value $M_z(0)$, rapidly at first and then increasingly slowly, and ceased to be detectable after 200 ps. When the normalized decay of the angular momentum, $M_z/M_z(0)$, averaged over the 35 runs (Fig. 6), was forced to fit a single exponential, it yielded a relaxation time $\tau_0 \simeq$ 83 ps (decay to $1/e$ of the initial value).

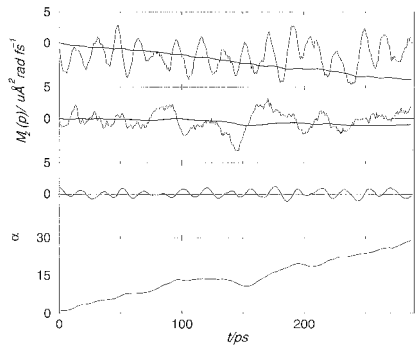

Fig. 3. Runs 6 and 7 in Table 1 (*A* and *B* in Fig. 2). (*Upper*) Instantaneous angular momentum and its integral (bold line). (*Lower*) Instantaneous lag angle $\alpha(t)$.

Discussion

An ideal simulation of the rotor would run forever, $t_{tot} = \infty$. In this limit, synchronous rotation (m = 0) would be characterized by a = 0 and $\nu_{rot} = \nu$, but we accept values up to $a = 1/e$ as synchronous. The quantities ⟨α⟩, ⟨$\delta\alpha$⟩, ⟨sinα⟩, and ⟨cosα⟩ would be physically meaningful measures of the average lag angle, its fluctuation, the average torque, and the average alignment of the dipole with the rotating field, respectively. Asynchronous rotation ($m \neq 0$) would be characterized by $1 > a > 0$ ($1 > a > 1/e$), and $\nu_{rot} < \nu$, where a provides a measure of the probability with which the rotor skips a turn of the field and raises the total lag angle α_{tot} by 2π. If the probability that the rotor breaks off in a single turn (and loses memory of this event before the next turn) is P, $a = P + \alpha/2\pi n \simeq P$. In the thermal regime, ν_{rot} would approach zero and a would approach unity. Our simulations are not converged in the statistical sense, causing a scatter of the results around the values expected for $t_{tot} = \infty$ (Table 1).

Table 2. Critical (E_c) and break-off (E_{bo}) field strengths (kV·cm^{-1}) and friction coefficient η_1 (eVps)

ν/GHz	E_c	E_{bo}	η_1	ν/GHz	E_c	E_{bo}	η_1
3	350*	150*	0.00229	110			0.09601
7.5			0.00169	120	2,100‡	1,000§	
10	400*	150*		130			0.09671
15			0.00503	150	3,000¶	2,500‡	0.18339
20	500†	200†					
30			0.00961	170			0.20926
40	600†	200†					
50			0.01150	190			0.19185
70			0.06244	200	4,500¶	2,800‖	
80	1,250‡	500†		210			0.23641
90			0.12573	250			0.22657

*± 100.
†± 150.
‡± 400.
§± 300.
¶± 500.
‖± 800.

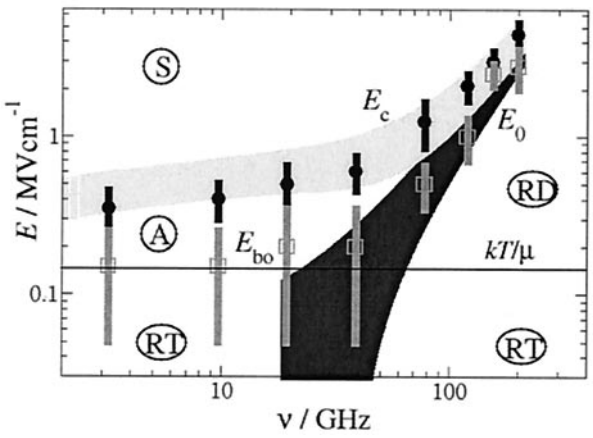

Fig. 5. Critical (E_c) and break-off (E_{bo}) field strength from simulations (dark and light points, respectively) and critical (E_c) and zero-temperature limit break-off (E_0) field strength from the model given by Eqs. **4–6** with η/eVps = 1.14 ν/THz (light and dark band, respectively). The bars on points and the thickness of the bands indicate estimated uncertainties. Four regions of rotation regimes are labeled: S, synchronous; A, asynchronous; RD, random driven; RT, random thermal.

A Simple Model. The results are compatible with intuitive expectations based on a simple classical model, which invokes friction and random thermal motion as the two factors opposed to synchronous rotation.

The limit of zero temperature and/or high field. For negligible thermal motion ($T \to 0$ and/or $E \to \infty$), the lag angle $\alpha(t)$ is determined by friction. In a stationary state, the value of $\alpha(t) = \alpha_0$ will be such that the rotor driving torque $\boldsymbol{E} \times \boldsymbol{\mu}$ compensates the drag torque, $-\boldsymbol{E} \times \boldsymbol{\mu} = \eta\boldsymbol{\omega}$, where the angular frequency $\boldsymbol{\omega}$ is viewed as a vector and η is the friction constant. Therefore,

$$\sin\alpha_0 = 2\pi\eta\nu/\mu E. \qquad [1]$$

If $\alpha_0 < \pi/2$, the rotor does not break off at all ($a = 0$). As E is reduced or ν increased and the lag angle α_0 attains the critical value of $\pi/2$, the break-off point is reached, and friction prevents synchronous rotation ($a = 1$). For a frequency independent η, the break-off frequency ω_0 would be proportional to field strength, $\omega_0 = E\mu/\eta$, and the zero-temperature field strength E_0, below which the rotor no longer follows the rotating field at zero

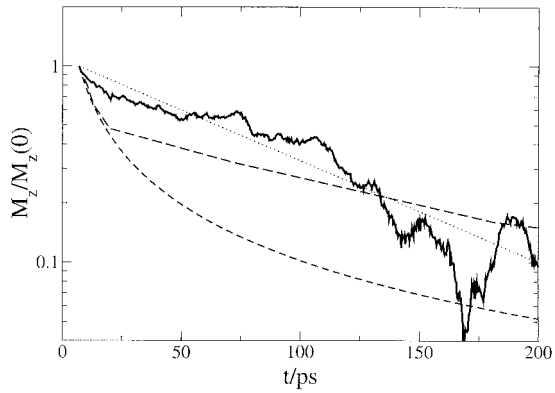

Fig. 6. Field-free decay of normalized angular momentum $\langle M_z(t)/M_z(0)\rangle$ after 155 GHz rotational excitation (average of 35 trajectories). $M_z(0)$ is the initial angular momentum. Dotted line: exponential fit (τ_0 = 83 ps). Long dash: decay calculated from η_1 obtained by independent fitting at 15 frequencies. Short dash: decay calculated from η_{1L} fitted assuming proportionality to ν.

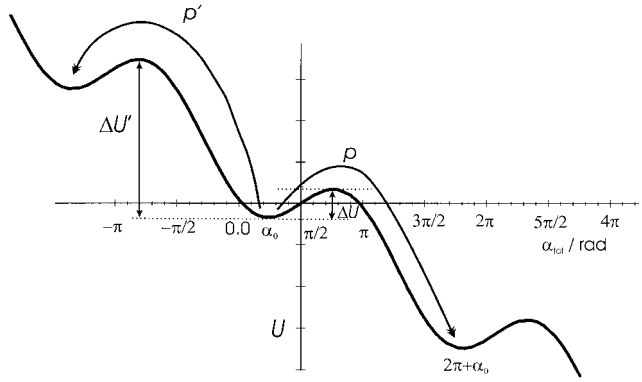

Fig. 7. Potential energy of an electric field-driven rotor in a rotating coordinate system.

temperature, would be proportional to frequency (at $T = 0$, $E_{bo} = E_c = E_0$):

$$E_0 = (\eta/\mu)\omega = (2\pi\eta/\mu)\nu;\ a = 0 \text{ if } E > E_0,\ a = 1 \text{ otherwise.} \qquad [2]$$

The approximately quadratic high-field limit frequency dependence of E_{bo} and E_c observed at 150 K therefore suggests that for our rotor η is proportional to frequency.

Finite temperature and field. Above absolute zero and at driving electric fields that are not excessively strong, the lag angle α fluctuates about its mean value $\langle\alpha\rangle$. As E is reduced, the instantaneous value of α reaches the critical value of $\pi/2$ at a temperature-dependent rate even before $\langle\alpha\rangle$ reaches $\pi/2$, and the rotor misses a turn. Because at $T > 0$ there is always a nonzero probability of skipping a turn, the break-off field E_{bo} at which a begins to deviate noticeably from unity is larger than E_0, and the critical field E_c, where it drops to $1/e$, is even larger. The ratio E_c/E_{bo} is a measure of the abruptness of the transition from perfect rotor behavior to irregular motion and should increase with temperature. It seems to be largely independent of ν.

The rotor also may gain an extra turn during a favorable thermal fluctuation. Its potential energy U is the sum of a friction term $U_f = -\eta\omega\alpha$ and a polarization energy term $U_p = E\mu\cos\alpha$. A plot of U against the lag angle in a coordinate system rotating at angular velocity ω exhibits a minimum on the potential energy surface at a value α_0 defined by Eq. **1**, and a maximum at the lag angle $\pi/2 + \alpha_0$, and is periodic (Fig. 7). When a turn is missed the rotor lag angle α moves from stationary position α_0 to a new stationary position $\alpha_0 + 2\pi$, initially against the force exerted by the electric field, and when a turn is gained, it moves from α_0 to $\alpha_0 - 2\pi$. The activation energies ΔU and $\Delta U'$ are

$$\begin{aligned} \Delta U &= 2[E\mu\cos\alpha_0 + \eta\omega(\pi/2 - \alpha_0)]; \\ \Delta U' &= 2[E\mu\cos\alpha_0 + \eta\omega(3\pi/2 - \alpha_0)]. \end{aligned} \qquad [3]$$

The rates p and p' at which α moves from α_0 to the critical value $\alpha_0 + \pi/2$ or $\alpha_0 - \pi/2$, thus causing a turn to be missed or gained in unit time, respectively, are assumed to be

$$p = A\exp(-\Delta U/kT);\ p' = A\exp(-\Delta U'/kT);\ A = 10^{-13}\ \mathrm{s}^{-1}. \qquad [4]$$

The probability of skipping a turn per field revolution is $a \simeq m/n$, where $m = (p - p')t$ is the number of missed turns and $n = t\nu$ is the total number of field turns. Assuming a dead time $t_{dead} = 1/\nu$ for each hopping event during which the rotor may not start skipping another turn, the total dead time is m/ν and thus the corrected number of missed turns is $m = (p - p')(t - t_{dead}) =$

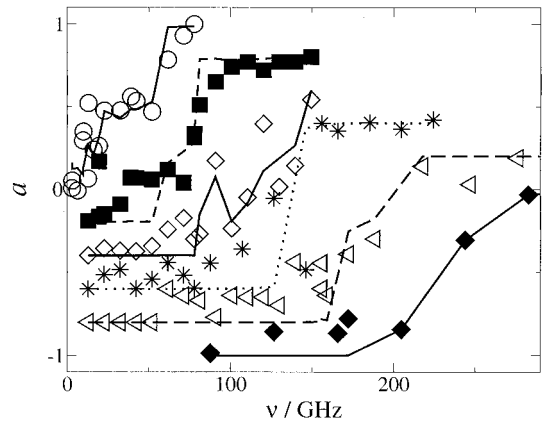

Fig. 8. Average lag per turn *a* from simulations (points) and from Eqs. **3-5** with $\eta_1(\nu)$ fitted separately in 15 frequency regions, using the actual average rotor temperatures for each run (lines). *E* in kV·cm^{-1}: 434 (○), 868 (■), 1,519 (◇), 2,170 (*), 3,472 (◁), and 5,280 (◆). Successive plots are displaced downward by 0.2.

$(p - p')(t - m/\nu)$, which leads to $m = (p - p')t\nu/[\nu + (p - p')]$ and

$$a \simeq m/n = (p - p')/[\nu + (p - p')] \text{ if } E > E_0; a = 1 \text{ if } E \leq E_0. \quad \textbf{[5]}$$

Eq. **5** does not yield a simple analytical formula for the critical field strength E_c, and E_{bo} has not been uniquely defined mathematically. In the limit $T \to 0$, Eq. **5** reverts to Eq. **2**. In the limit $E \to E_0$ and $2\pi\eta\omega \gg kT$, $a \to A/(A + \nu)$, which causes a discontinuity with the result $a = 1$ valid for $E \leq E_0$. This is not significant if $A \gg \nu$, but the model cannot be used when $A \simeq \nu$.

The friction coefficient. The effective friction coefficient η of the rotor was derived in four ways, denoted η_1–η_4.

The $a(E,\nu,T)$ values from all 171 molecular dynamics simulations (Table 1, *cf.* points in Fig. 4) were fitted to Eqs. **3–5** using an adaptive nonlinear least-squares algorithm (33), yielding η_1. Because we could not fit the data with a single friction constant independent of ν, we divided the frequency range into 15 intervals with an independent value of η_1 in each. The $a(E,\nu)$ values from the simulations (Fig. 8) and the frequency dependence of $E_{bo}(\nu)$ and $E_c(\nu)$ were fitted very well. The resulting values of $\eta_1(\nu)$ (Table 2) are approximately proportional to ν (Fig. 9), as anticipated from the discussion of the high-field limit, $\eta_1/\text{eVps} \simeq 1.1\ \nu/\text{THz}$. Below ~50 GHz friction is much smaller and is better described by $\eta_1/\text{eVps} \simeq 0.2\ \nu/\text{THz}$. Apparently, the coupling between the rotor rotational motion and vibrational modes of the grid increases at frequencies above ~50 GHz.

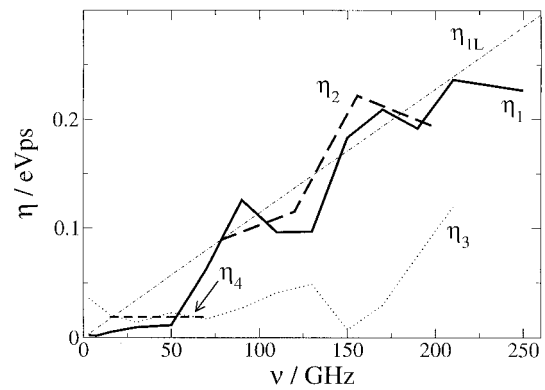

Fig. 9. Friction coefficient $\eta(\nu)$ derived in four different ways (see text); η_{1L} was obtained by assuming direct proportionality between η and ν.

When exact proportionality between η_1 and ν was assumed and the proportionality coefficient was treated as the only adjustable parameter in the least-squares fitting of the 171 $a(E,\nu)$ values, the result was $\eta_{1L}/\text{eVps} \simeq 1.14\ \nu/\text{THz}$ (Fig. 9). The fit was now worse but still respectable, and the fit of the $E_c(\nu)$ curve was still excellent (Fig. 5). With η_{1L} proportional to ν, the frequency dependence of E_0, the zero-temperature limit of the break-off field calculated from Eq. **2**, becomes linear in the log-log plot of Fig. 5, with a slope of two. In high-field limit the finite temperature break-off field strength curve $E_{bo}(\nu)$ fits it asymptotically very nicely. In the low-field limit, $E_{bo}(\nu)$ becomes frequency-independent as it approaches kT/μ.

Above 40 GHz (where $E_0\mu \simeq kT$), friction dominates and E_{bo} can be identified with the value E_0 in Eq. **2**, yielding $\eta_2(\nu)$, in fair agreement with $\eta_1(\nu)$ (Fig. 9).

To obtain η_3, the sine of the lag angle is identified with the mean value $\langle\sin\alpha\rangle$ obtained in the simulation. According to Eq. **1**, $2\pi\eta_3/\mu$ is equal to the slope of the plot of $\langle\sin\alpha\rangle$ against ν/E when α is dictated by friction and not by thermal fluctuations. We selected 58 runs in which the rotor followed the field most of the time ($\langle\sin\alpha\rangle > 0.0$, $0.0 < a < 0.23$) and calculated η_3 for 15 frequencies (Fig. 9). The plot of $\langle\sin\alpha\rangle$ shows considerable scatter (Fig. 4), and the resulting η_3 is very inaccurate. Unlike η_1, η_{1L}, and η_2, it is almost frequency independent. It has a low average value of 0.024 eVps, perhaps because the effective friction constant for these selected runs differs from the rest. We do not consider η_3 reliable.

The rate of decay of $\langle M_z\rangle$ in the absence of the driving field was used to estimate η_4 from $\tau_0 = I/\eta_4$. A fit to a single exponential (Fig. 6) yields $\eta_4 = 0.019$ eVps in the region of low frequencies examined, very close to η_1 and η_3 (Fig. 9; in this region η_2 is not available). The decay curve expected from η_1 indeed agrees quite well with that obtained from the molecular dynamics runs (Fig. 6). The much faster decay observed for η_{1L} reflects the overestimation of its value relative to η_1 in the frequency region below 50 GHz (Fig. 9).

The cause of friction. All of the determinations of η suffer from statistical uncertainties in the trajectory calculations. The friction constant η_1 is probably the most realistic, because even in the synchronous motion limit the rotor fluctuates around the direction of the field. The friction constant may depend on field strength and temperature, but we were unable to prove such dependence.

The friction is attributed to a kinematic and electric-field coupling of the rotor rotational states to the vibrational and rotational state manifold of the molecular grid. As ν increases, it enters the region of an increasing density of grid states and the coupling to the grid becomes stronger, causing higher friction. It is possible that the plot of η against ν contains specific resonances with particularly strongly coupled low-frequency bending modes of the grid, but our calculations are not accurate enough to reveal them unambiguously. The fact that $\eta_1(\nu)$ is very small at low frequencies suggests that at lower temperatures it may be possible to rotate the rotor synchronously at even lower frequencies using weaker fields, as long as the rotational barrier is low.

Langevin Dynamics. Numerically integrated Langevin dynamics including a stochastic force (34) would provide a more accurate model. The Langevin equations of Brownian motion are identical with the equations (35) describing the current-voltage characteristics of a Josephson junction (JJ), with the the JJ current variable *i* defined by $i = \omega/\omega_0$. The JJ voltage *V* relative to the current *i* can be expressed as $V/i = \langle d\alpha/dt\rangle/\omega \approx \alpha_{tot}/(t_{tot}\omega) = a$. For our rotor the usual McCumber parameter β_C and thermal parameter γ are $\beta_C = E\mu I\eta^{-2}$ and $\gamma =$

$2\pi kT(E\mu)^{-1}$. Many numerical results for JJ plots have been published, but we found little information for the parameter values relevant for our rotor, $14 < \beta_C < 140$ and $0.17 < \gamma < 2$. Numerical solutions (36) of the Langevin equation for JJ circuits with $\beta_C = 1$ and 4, and $\gamma = 10$, and experimental observations (37) in a similar range yielded $i - V$ plots (figure 1 in ref. 36 and figure 11 in ref. 37) in qualitative agreement with our $a - \nu$ plots, which correspond to $V/i - i$. For $\beta_C \simeq 4$, the JJ results predict that the motion of our rotor will be hysteretic: once regular rotation is induced by an above-critical electric field, the field will have to be reduced to about 70% of the critical value before the rotor fails.

Synchronous, Asynchronous, Random Driven, Random Thermal, and Hindered Regimes of Rotation. We anticipate five regimes of molecular rotor behavior dictated by the relative importance of random thermal forces described by kT, of the strength (μE) of maximum rotor-field interaction, the friction constant η that describes the break-off drag torque, and the rotational barrier height W. Presently, we have investigated four of them.

Synchronous rotor regime. When $\mu E > \mu E_c, kT, W$, the rotor follows the rotating field slavishly and rotates at its frequency ν (points above the E_c line in Fig. 5).

Asynchronous rotor regime. When $\mu E_c > \mu E > \mu E_{bo}, kT, W$, the rotor turns at a frequency lower than ν because it occasionally skips a turn (points between the E_c and E_{bo} curves in Fig. 5). The decrease of the ratio of the averaged rotational frequency of the rotor to that of the field is abrupt (Fig. 4). Even for a values close to unity the rotor still rotates significantly.

Random driven rotor regime. When $\mu E_c, \mu E_{bo} > \mu E > kT, W$, friction is excessive. The rotor cannot keep up with the rotating field and performs irregular motion (points below the E_{bo} curve and above the kT/μ line in Fig. 5).

Random thermal rotor regime. When $kT > \mu E, W$, the rotor exhibits nearly random thermal fluctuations with a slight preference for rotation in the sense of the rotating field (points below the kT/μ line in Fig. 5; at $T = 150$ K, μE equals kT at $E = 140$ kV·cm^{-1}). The independence of E_c and E_{bo} of ν in the limit of low frequencies is unlike anything observed for macroscopic rotors at ordinary temperatures. Molecular dynamics investigation of this regime is unlikely to offer significant advantages over a purely statistical description (19) (a freely rotating dipolar solute in a solvent of relaxation constant Γ has an average angular velocity $(\omega/2)[1 + (\omega/\Gamma)^2]^{-1}$ $(\mu E/kT)^2$ to second order in $\mu E/kT$.

Hindered rotor regime. When $W > kT, \mu E$, the rotor will jump infrequently from one to another minimum on the potential energy surface. At 150 K, $kT = 0.3$ kcal/mol, which is comparable with our estimate of the barrier height W. As a result, for $E < \sim 140$ kV·cm^{-1}, the effect of the barrier, and possibly also quantization effects, will have to be included in the modeling. Our simulations have been performed at $kT \geq W$ or at a higher field strength, and we do not address this issue.

Conclusions

Molecular dynamics simulations and simple modeling provide a detailed view of the interplay of the driving force, friction, and thermal motion acting on a dipolar molecular rotor, likely to be informative for "single-molecule machines" in general. The regimes examined at 150 K range from macroscopic (synchronous or random driven rotor) to molecular (random thermal rotor). The derived phenomenological friction constant should facilitate studies of dipolar rotor arrays.

We are grateful to Prof. John C. Price for a helpful discussion. This project was supported by the National Science Foundation (CHE-9871917), the European Office of Aerospace Research and Development (SPC-98-4031), the J. Heyrovský Institute, and the Grant Agency of the Academy of Sciences of the Czech Republic (B4040006/00).

1. Kaszynski, P. & Michl, J. (1988) *J. Am. Chem. Soc.* **110,** 5225–5226.
2. Michl, J., Kaszynski, P., Friedli, A. C., Murthy, G. S., Yang, H.-C., Robinson, R. E., McMurdie, N. D. & Kim, T. (1989) in *Strain and Its Implications in Organic Chemistry*, eds. de Meijere, A. & Blechert, S. (Kluwer, Dordrecht, The Netherlands), NATO Advanced Science Institutes Series, Vol. 273, p. 463–482.
3. Magnera, T. F., Peslherbe, L. M., Körblová, E. & Michl, J. (1997) *J. Organomet. Chem.* **548,** 83–89.
4. Kaszynski, P., Friedli, A. C. & Michl, J. (1992) *J. Am. Chem. Soc.* **114,** 601–620.
5. Magnera, T. F., Pecka, J., Vacek, J. & Michl, J. (1997) in *Nanostructural Materials: Clusters, Composites, and Thin Films*, eds. Moskovits, M. & Shalaev, V. (Am. Chem. Soc., Washington, DC), ACS Symposium Series 679, pp. 213–220.
6. Magnera, T. F., Pecka, J. & Michl, J. (1998) in *Science and Technology of Polymers and Advanced Materials*, eds. Prasad, P. N., Mark, J. E., Kandil, S. H. & Kafafi, Z. H. (Plenum, New York), pp. 385–391.
7. Harrison, R. M., Magnera, T. F., Vacek, J. & Michl, J. (1997) in *Modular Chemistry*, ed. Michl, J. (Kluwer, Dordrecht, The Netherlands), pp. 1–16.
8. Koumura, N., Zijlstra, R. W. J., van Delden, R. A., Harada, N. & Feringa, B. L. (1999) *Nature (London)* **401,** 152–155.
9. Bedard, T. C. & Moore, J. S. (1995) *J. Am. Chem. Soc.* **117,** 10662–10671.
10. Kelly, T. R., Tellitu, I. & Sestelo, J. P. (1997) *Angew. Chem. Int. Ed. Engl.* **36,** 1866–1868.
11. Gimzewski, J. K., Joachim, C., Schlittler, R. R., Langlais, V., Tang, H. & Johannsen, I. (1998) *Science* **281,** 531–533.
12. Clayden, J. & Pink, J. H. (1998) *Angew. Chem. Int. Ed. Engl.* **37,** 1937–1939.
13. Balzani, V., Gómez-López, M. & Stoddart, J. F. (1998) *Acc. Chem. Res.* **31,** 405–414.
14. Sauvage, J. P. (1998) *Acc. Chem. Res.* **31,** 611–619.
15. Bermudez, V., Capron, N., Gase, T., Gatti, F. G., Kajzar, F., Leigh, D. A., Zerbetto, F. & Zhang, S. (2000) *Nature (London)* **406,** 608–611.
16. Villeneuve, D. M., Aseyev, S. A., Dietrich, P., Spanner, M., Ivanov, M. Y. & Corkum, P. B. (2000) *Phys. Rev. Lett.* **85,** 542–545.
17. Rozenbaum, V. M., Ogenko, V. M. & Chuiko, A. A. (1991) *Sov. Phys. Usp.* **34,** 883–902.
18. Noji, H., Yasuda, R., Yoshida, M. & Kinoshita, K., Jr. (1997) *Nature (London)* **386,** 299–302.
19. Baranova, N. B. & Zel'dovich, B. Y. (1978) *Chem. Phys. Lett.* **57,** 435–437.
20. Space, B., Rabitz, H., Lörincz, A. & Moore, P. (1996) *J. Chem. Phys.* **105,** 9515–9524.
21. Astumian, R. D. (1997) *Science* **276,** 917–922.
22. Vacek, J. & Michl, J. (1997) *New J. Chem.* **21,** 1259–1268.
23. Zorski, H. & Infeld, E. (1992) *Phys. Rev. Lett.* **68,** 1180–1183.
24. DeLeeuw, S. W., Solvaeson, D., Ratner, M. A. & Michl, J. (1998) *J. Phys. Chem. B.* **102,** 3876–3885.
25. Sim, E., Ratner, M. A. & de Leeuw, S. W. (1999) *J. Phys. Chem. B.* **103,** 8663–8670.
26. Marinari, E., Parisi, G. & Ruiz-Lorenzo, J. (1997) http://xxx.lanl.gov/abs/cond-mat/9701016.
27. Tuzun, R. D., Noid, D. W. & Sumpter, B. G. (1995) *Nanotechnology* **6,** 52–63.
28. Sohlberg, K., Tuzun, R. E., Sumpter, B. G. & Noid, D. W. (1997) *Nanotechnology* **8,** 103–111.
29. Rappé, A. K., Casewit, C. J., Colwell, K. S., Goddard, W. A., III, & Skiff, W. M. (1992) *J. Am. Chem. Soc.* **114,** 10024–10035.
30. Rappé, A. K. & Goddard, W. A., III (1991) *J. Phys. Chem.* **95,** 3358–3363.
31. Dunbar, K. R. (1988) *J. Am. Chem. Soc.* **110,** 8247–8249.
32. Cotton, F. A. & Walton, R. A. (1993) *Multiple Bonds Between Metal Atoms* (Clarendon, Oxford), pp. 431–501, 2nd Ed.
33. Dennis, J. E., Gay, D. M. & Welsch, R. E. (1981) *Acm. Trans. Math. Software* **7,** 348–369.
34. Madura, J. D., Briggs, J. M., Wade, R. C. & Gabdoulline, R. R. (1998) in *Encyclopedia of Computational Chemistry*, eds. Schleyer, P. v. R., Allinger, N. L., Clark, T., Gasteiger, J., Kollman, P. A., Schaefer, H. F., III, & Schreiner, P. R. (Wiley, Chichester, United Kingdom), Vol. 1, pp. 141–154.
35. Barone, A. & Paternò, G. (1982) *Physics and Applications of the Josephson Effect* (Wiley, New York).
36. Kurkijärvi, J. & Ambegaokar, V. (1970) *Phys. Lett. A* **31,** 314–315.
37. Falco, C. M., Parker, W. H., Trullinger, S. E. & Hansma, P. K. (1974) *Phys. Rev. B* **10,** 1865–1873.